Materials & Design 214 (2022) 110422

Contents lists available at ScienceDirect

Materials & Design

journal homepage: www.elsevier.com/locate/matdes

Tetragonal distortion in magnetron sputtered bcc-W films with supersaturated carbon

B.O. Mukhamedov [a,*], S. Fritze [b], M. Ottosson [b], B. Osinger [b], E. Lewin [b], B. Alling [a], U. Jansson [b], I.A. Abrikosov [a,c]

[a] Theoretical Physics Division, Department of Physics, Chemistry and Biology (IFM), Linköping University, SE-581 83 Linköping, Sweden
[b] Department of Chemistry-Ångström, Uppsala University, Box 538, SE-75121 Uppsala, Sweden
[c] Materials Modeling and Development Laboratory, National University of Science and Technology 'MISIS', 119049 Moscow, Russia

HIGHLIGHTS

- X-ray diffraction experiments show that W films supersaturated with C (2 and 4 at.%) exhibit a tetragonal distortion.
- Level of tetragonal distortion in W-C films increases with C content.
- Maximum distortion (c/a = 1.02) at 4 at.% C with a = 3.15–3.16 Å, c = 3.21–3.22 Å.
- DFT calculations show that the body centered tetragonal structure has a lower mixing energy than the bcc structure.
- Calculated E-modulus decreases with increased C content from 405 GPa to 385 GPa and experiments follow the same trend.

GRAPHICAL ABSTRACT

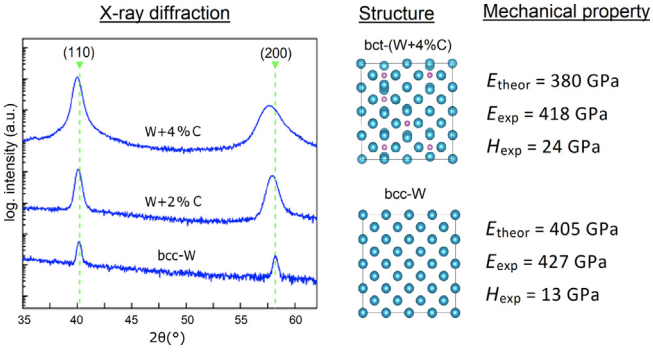

ARTICLE INFO

Article history:
Received 12 November 2021
Revised 18 January 2022
Accepted 21 January 2022
Available online 24 January 2022

Keywords:
Tungsten
Supersaturated solid solution
Thin film diffraction
Density functional theory
Thermodynamic stability
Elastic property

ABSTRACT

Carbon has a low solid solubility in bcc tungsten at equilibrium. However, metastable supersaturated solid solutions can be synthesized with magnetron sputtering. Here, we present a systematic study on the phase stability and mechanical properties of such supersaturated W–C solid solutions. Θ–2θ scans show a split of the 200/020 and the 002 peaks for supersaturated films which is explained by a tetragonal distortion of the bcc structure. This split increases with increasing C content and is maximized at 4 at.% C, where we observe an a/b axis of 3.15–3.16 Å and a c-axis of 3.21–3.22 Å. We performed first-principles calculations of lattice parameters, mixing enthalpies, elastic constants and polycrystalline elastic moduli for cubic and tetragonal W–C solid solutions. Calculations show that tetragonal structure is more stable than the bcc supersaturated solid solution and the calculated lattice parameters and Young's moduli follow the same trends as the experimental ones as a function of C concentration. The results suggest that supersaturated films with lattice distortion can be used as a design approach to improve the properties of transition metal films with a bcc structure.

* Corresponding author.
E-mail address: boburjon.mukhamedov@liu.se (B.O. Mukhamedov).

https://doi.org/10.1016/j.matdes.2022.110422
0264-1275/

1. Introduction

Tungsten (W) has a combination of technologically attractive properties such as a high melting point [1], a high strength at high temperature [2], and resistance to radiation damage [3,4]. This makes W a suitable candidate material for harsh environments in, for example, nuclear and fusion reactors [5,6]. The properties of W can be further enhanced by alloying with other metals such as rhenium or by the addition of p-elements such as carbon (C) and boron [7–9]. The solubility of C in body centered cubic (bcc) W is ~ 1 at.% at 2700 °C and far below 0.5 at.% at room temperature [10]. The effect of C in W on the phase formation, the mechanical and radiation properties has been studied at concentrations below the solubility limit (<1 at.%) [11–13].

An alternative route to design the properties of W is to add p-elements such as C to concentrations above the solubility limit. Such metastable structures are difficult to obtain in conventional materials synthesis such as casting but is frequently observed in thin films deposited with magnetron sputtering [14–16]. This can be explained by the high quenching rates during the sputter process, which reduces the surface diffusion length and makes it difficult to nucleate thermodynamically stable phases with a very different chemical composition and structure compared to a supersaturated solid solution [17]. Supersaturated W films has been observed in several studies leading to twice as hard coatings compared to pure W [14–16]. In a recent study, we have investigated the effect of C on the mechanical properties and microstructure of sputtered bcc W films with ~ 2 at.% and ~ 4 at.% of C [18]. No carbide or carbon clusters were formed in these films according to atom probe tomography (APT) measurements [19]. Micropillar compression tests revealed that the flow stress increased from ~ 3.8 to ~ 8.3 GPa upon the C addition and no material embrittlement was observed [18].

The very low maximum solubility of carbon in transition metals with a bcc structure compared to face centered cubic (fcc) metals can be explained by the small size of the interstitial sites in the bcc structure [20]. The most well-known example is Fe, where the fcc phase (austenite) at higher temperatures has a significantly higher solubility of carbon than the low-temperature bcc phase (ferrite). With high quenching rates, the formation of a carbide phase is suppressed and martensite is formed. This phase can be described as a tetragonal distortion of the bcc lattice. An obvious question is therefore if also other transition metals with supersaturated carbon such as W can form a tetragonally distorted lattices. Theoretical studies of the Bain/tetragonal distortion path for pure W have shown that the energy for such distortion is high [21]. However, experimental evidence for a tetragonal distortion was observed by Palmquist et al. [13] and also from XRD analyses in Ref. [18]. The aim of this paper is to investigate if such tetragonal distortion is present also in supersaturated W films using density functional theory (DFT) simulations combined with detailed experimental studies of carbon-containing films with X-ray diffraction using ψ–2θ mapping.

2. Methodology

2.1. Thin film deposition and characterization

The W–C films were synthesized by non-reactive magnetron sputtering from elemental targets using a Qprep500i (Mantis Deposition Ltd.) system. The α-Al_2O_3 (000l) substrates were heated to 300 °C and the films were deposited to a thickness of about 4.5 μm with a deposition rate of ~ 600 nm/h. A detailed description of the deposition conditions is published in Ref. [18].

The chemical composition of the films was determined by Time-of-Flight Energy elastic recoil detection analysis (ToF-E-ERDA) 36 MeV $^{127}I^{8+}$ (iodine) and 32 MeV $^{35}Cl^{7+}$ (chlorine). Details of the ERDA analysis can be found in Ref. [14]. The composition of the sample with the highest concentration of C was further confirmed by atom probe tomography (APT) [19].

Texture scans and ψ–2θ maps were measured with a Philips MRD Pro equipment using CuKα radiation, operating in point focus with a proportional Xe gas filled detector. A capillary lens was used as primary optic, with a beam size of 2 × 2 mm^2. As secondary optic a 0.18° parallel plate collimator with graphite monochromator was used. The ψ–2θ maps are made from θ–2θ scans for each individual value of ψ. Θ–2θ scans at a fixed ψ angels were analyzed to determine the 2θ positions of the individual peaks. A Philips MRD Pro with pure CuKα1 radiation, operating in line focus mode, was used for reciprocal space mapping (RSM). A hybrid 2-bounce monochromator was used as primary and an X-ray mirror in combination with a 0.1 mm receiving slit were used as secondary optics. A Xe gas filled detector was also used for the RMS.

2.2. DFT calculations

The DFT calculations were performed using the projector augmented wave method [22] implemented in the VASP software [23–25]. The generalized gradient approximation [26] was used to describe the exchange and correlations effects. The cutoff energy for plane waves was set to 450 eV. The convergence criterion for electronic subsystem was set to 10^{-4} eV for subsequent iterations. The relaxation of atomic positions was carried out by calculating the Hellman-Feynman forces [27] and the stress tensor and using them in the conjugated gradient method. Relaxation was completed when the forces on the ions became of the order of 10^{-2} eV/Å. We have performed full lattice relaxation for W–C supercells, which includes the relaxation of volume, shape and ions. The integration over the irreducible part of Brillouin zone was carried out using the Monkhorst-Pack method [28] on a grid of 3 × 3 × 3 *k* points. All calculations were performed for the 4 × 4 × 4 cubic supercell of W (128 atoms). First, for the single carbon impurity we performed test calculations by placing single C atom in both tetrahedral and octahedral interstitial positions in the W supercell. The test reviled that tetrahedral coordination for C is not stable, and with ionic relaxation the C impurity migrates to the nearest octahedral position. Therefore, for the further calculations we considered only octahedral coordination for C atoms. In the bcc lattice the centers of octahedral sites can be defined by the pair of the nearest tungsten atoms (see Fig. 1): there are 3 octahedral interstitial sites per one W atom, and the corresponding three pair of the nearest W atoms to these sites are oriented along three crystallographic directions *x*, *y* and *z*. As for the 4 × 4 × 4 W supercell, there are 128 octahedral sites along each direction, i.e. 384 octahedral sites in total.

In simulations of a W–C solid solution, one can consider the sublattice of interstitial sites as a system randomly occupied by carbon atoms and vacancies. In this work we consider three different configurations for carbon atoms in bcc supercell. The first configuration of W–C supercells is fully tetragonal where the carbon atoms randomly occupy only *z* interstitial sites. This leads to tetragonal distortion of lattice with *c*/*a* ratio > 1. In the second configuration of W–C supercells, which is cubic, the carbon atoms equally but randomly occupy all three *x*, *y* and *z* interstitial sites. Thus, in the cubic configuration there is almost no global distortion of the supercell, and $c/a \approx 1$. The third considered configuration of W–C supercell is partially tetragonal where half of C atoms occupy *z* interstitial sites and the other half equally occupy *x* and *y* interstitial sites atoms. The random distribution of C atoms in the interstitial sites was realized within the special quasirandom structure

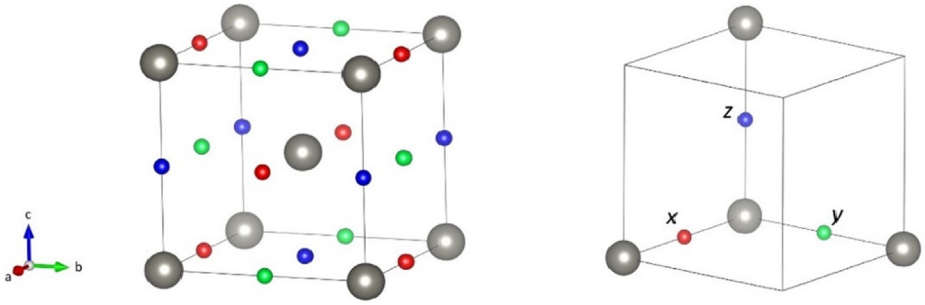

Fig. 1. Schematic illustration of octahedral interstitial positions in bcc tungsten. The red, green and blue spheres indicate centers of x, y and z interstitial sites, respectively.

method (SQS) [29]. For fully tetragonal and cubic W–C solid solutions we generated the SQSs with two concentrations of carbon: 2.29 at.% (128W + 3C) and 4.48 at.% (128W + 6C). As for the partially tetragonal configuration, we generated additional SQS with 3.03 at.% C (128W + 4C) since the number of C atoms should be the multiple of four.

The mixing enthalpy of W–C solid solutions was defined with reference to pure W and graphite, and also with reference to pure W and stochiometric tungsten carbide WC, as:

$$H_{mix}^{graphite}(C) = E_{W+C} - \frac{N_W \cdot E_W + N_C \cdot E_C}{N_W + N_C} \quad (2)$$

$$H_{mix}^{carbide}(C) = \frac{(N_W + N_C) \cdot E_{W+C} - N_C \cdot E_{WC} - (N_W - N_C) \cdot E_W}{N_W + N_C} \quad (3)$$

where N_W and N_C indicate the number of tungsten and carbon atoms in the supercell, respectively. The E_{W+C}, E_W, E_C, E_{WC} denote the total energies (per atom) of the W–C supercell, pure tungsten, graphite and WC carbide, respectively. The energies in Eqs. (2) and (3) correspond to the ground state volumes, when the external pressure is zero. The total energy calculation for graphite E_C was performed using experimental lattice parameters (a = 2.46 Å, c = 6.65 Å) [30]. For the tungsten carbide WC, we considered the hexagonal structure which at the ground state has lattice parameters a = 2.92 Å and c = 2.84 Å.

The bulk moduli of all SQSs were defined according to Birch-Murnaghan equation of states (EOS) [31]. The EOS calculations were performed for 7 volume points in the range ± 3% with respect to the ground state volume. The single crystal elastic constants were defined via energy-strain relation. External strain applied to equilibrium lattice leads to the lattice distortion that can be represented as [32]:

$$\begin{pmatrix} a' \\ b' \\ c' \end{pmatrix} = (I + \epsilon) \begin{pmatrix} a_0 \\ b_0 \\ c_0 \end{pmatrix} \quad (4)$$

where a_0, b_0 and c_0 are equilibrium lattice parameters; i denotes identity matrix and ϵ denotes the strain tensor, which is given in the following form [32]:

$$\epsilon = \begin{pmatrix} e_1 & e_6/2 & e_5/2 \\ e_6/2 & e_2 & e_4/2 \\ e_5/2 & e_4/2 & e_3 \end{pmatrix} \quad (5)$$

The energy change $\Delta E = E - E_0$ induced by infinite small elastic strain can be given by [32]:

$$\Delta E = \frac{V_0}{2} \sum_{i=1}^{6} \sum_{j=1}^{6} C_{ij} e_i e_j + O[e_i^3] \quad (6)$$

where V_0 denotes the equilibrium volume, C_{ij} denotes the second-order elastic constants, e_i and e_j are the components of strain tensor. Here, the cubic and the higher order terms in the expansion of the elastic energy ΔE are neglected.

The crystal with the cubic symmetry has three independent second-order elastic constants: C_{11}, C_{12} and C_{44}. While for the tetragonal crystal there are six independent elastic constants: C_{11}, C_{12}, C_{13}, C_{33}, C_{44} and C_{66}. Table 1 lists the strains tensors required to determine the elastic constants for cubic and tetragonal crystals: three and six strain tensors, respectively. The stain value applied to the lattices was set to δ = ±1 %, ±2 %. With information on the single-crystal elastic constants C_{ij} one can determine the polycrystalline elastic moduli using the Voight-Reuss-Hill averaging [34–36].

3. Results and analysis

3.1. Characterization of deposited films

Three different sets of films with 0 at.%, ~2 at.% and ~ 4 at.% C were deposited on Al_2O_3 substrates. In the following they will be named W, W2 and W4, respectively. Details on the microstructure of these films are given in Ref. [18] but a representative SEM cross-section of the W4 film is shown in Fig. 2a. All films have a columnar microstructure. The θ–2θ scans shown in Ref. [18] suggest that all films exhibit a strong <hh0> texture. The major effect of adding C is grain refining where the average column width decreased from ~ 133 nm in the carbon-free W film to ~ 20 nm in the W4 film. Furthermore, XRD and APT studies have shown that most of the carbon is dissolved in the bcc structure above the maximum solubility of > 1 at.% [10]. Magnetron sputtering occurs far from equilibrium and the atoms hitting the growing film are rapidly quenched. This reduces the diffusion lengths and makes it difficult to directly form multiphase films where the two phases have large differences in composition and structure. Hence, formation of

Table 1
Strain tensors used for calculations of elastic constants of cubic and tetragonal lattices [32,33]. Unlisted components of strain tensors are equal to zero.

Lattice	Strain type		Energy change $\Delta E/V_0$
Cubic	1	$e_1 = -e_2 = \delta$ $e_3 = \delta^2/(1-\delta^2)$	$(C_{11} - C_{12})\cdot\delta^2 + O[\delta^4]$
	2	$e_1 = e_2 = e_3 = \delta$	$\frac{3}{2}\cdot(C_{11} + 2C_{12})\cdot\delta^2 + O[\delta^4]$
	3	$e_3 = \delta^2/(4-\delta^2)$ $e_6 = \delta$	$\frac{1}{2}\cdot C_{44}\cdot\delta^2 + O[\delta^4]$
Tetragonal	1	$e_1 = e_2 = \delta$	$(C_{11} + C_{12})\cdot\delta^2 + O[\delta^3]$
	2	$e_1 = e_2 = \delta$ $e_3 = -\delta(2+\delta)/(1+\delta)^2$	$(C_{11} + C_{12} + 2C_{33} - 4C_{13})\cdot\delta^2 + O[\delta^3]$
	3	$e_1 = ((1+\delta)/(1-\delta))^{0.5} - 1$ $e_2 = ((1-\delta)/(1+\delta))^{0.5} - 1$	$(C_{11} - C_{12})\cdot\delta^2 + O[\delta^3]$
	4	$e_3 = \delta$	$\frac{1}{2}\cdot C_{33}\cdot\delta^2 + O[\delta^3]$
	5	$e_4 = e_5 = \delta$, $e_3 = \delta^2/4$	$C_{44}\cdot\delta^2 + O[\delta^4]$
	6	$e_6 = \delta$ $e_1 = e_2 = (1+\delta^2/4)^{0.5} - 1$	$\frac{1}{2}\cdot C_{66}\cdot\delta^2 + O[\delta^4]$

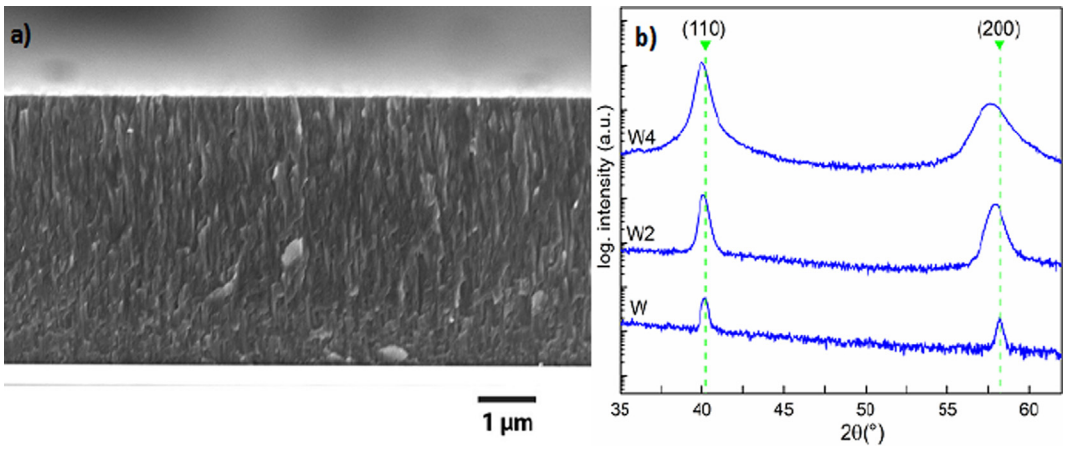

Fig. 2. (a) Cross section SEM of W4 film, and (b) grazing incidence X-ray diffraction pattern showing an asymmetric (200) peak indicating a distortion of the bcc lattice for the W2 and W4 film. Data reproduced from Ref. [18].

supersaturated (metastable) solid solutions is therefore not unusual in magnetron sputtering, see e.g., Ref. [37].

An interesting observation in Ref. [18] was that the (200) peak for the W2 and W4 films were asymmetric (see Fig. 2b), which could indicate a distortion of the cubic lattice. However, simple θ–2θ or grazing incidence (GI) scans cannot resolve such a distortion. We therefore analyzed the film with texture scans and ψ–2θ maps. These techniques are suitable for strongly textured films, as by tilting the sample in ψ, the non-surface planes can be measured. The problem with strongly textured films is otherwise that only the surface normal planes can be measured with standard θ–2θ scans. Furthermore, reciprocal space mapping (RSM) can be used for epitaxial as well as textured films, however, the number of peaks which are possible to measure is limited when ψ is set to zero [38]. With this technique, peaks from a tetragonal phase showing a 2θ separation of the 200/020 and the 002 peaks can be identified.

The lattice parameters for the three films are summarized in Table 2. The results confirm that the W films exhibit a strong epitaxial orientation on the Al_2O_3 (000l) substrate. The *a*/*b* axes were determined to 3.172 Å from θ–2θ scans of the 110/220 surface normal planes. Additionally, RSM maps, using the 110, 013 and the 222 plans, were measured to determine the *c*-axis to 3.16 Å. This small difference between *a*/*b* and *c* axis can probably be attributed to thermal strain. Also, the W2 film grows with a <hh0> texture but parts of the film were also <*h*00> textured, however, with a tilt of ± 18-22° from the surface normal. The lattice parameters were determined by measuring θ/2θ scans of the 110/220 surface normal plane and from ψ–2θ maps for the planes not normal to the surface. A small split in the *a*/*b* and *c* axis was observed in the ψ–2θ maps for the 200/020 and 002 peaks (see Fig. 3). This shift corresponds to a *a*/*b* axis of 3.17 Å and a *c*-axis of 3.19 Å (see Fig. 3b).

As can be seen in Fig. 3c the W4 film grows partly with a tilted (18-22°) <*h*00> texture with respect of the surface normal. Some parts of the film were also <hh0> textured [18]. Due to the tilt of the 100 orientations, θ–2θ scans shows low intensities of the

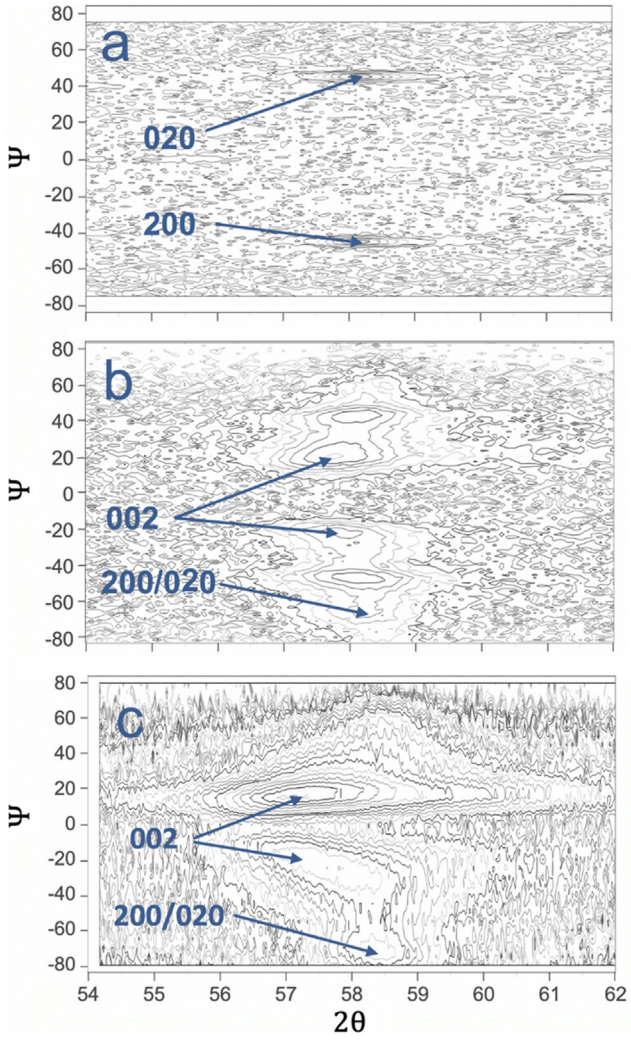

Fig. 3. ψ–2θ maps around 58° showing the 002 and 200 reflections, (a) W, (b) W2, and (c) W4.

Table 2
Lattice parameters for the W, W2 and W4 films determined by θ–2θ scans and ψ–2θ maps.

Film	*a*/*b* axis (Å)	*c*-axis (Å)	Method
W	3.172	3.16	RSM, θ–2θ scans
W2	3.17	3.18–3.19	ψ–2θ mapsθ–2θ scans
W4	3.15–3.16	3.21–3.22	ψ–2θ mapsθ–2θ scans

100/200 peaks. A split in the *a*/*b* and *c* axis was observed in the ψ–2θ maps for the 200/020 and 002 peaks (Fig. 3c); this shift corresponds to a *a*/*b* axis of 3.15–3.16 Å and a *c*-axis of 3.21–3.22 Å. The W films shows the 020/200 from the <hh0> texture tilted

45° (Fig. 3a) these peaks can also be seen for the W2 and W4 films. In summary, the experimental results confirm the presence of tetragonal distortion which seems to increase with higher carbon content.

3.2. Results of DFT calculations

The existence of a tetragonally distorted bcc structure in carbon supersaturated W was further explored with DFT calculations. As described in Section 2.2 (Fig. 1), the calculations were carried out using three different configurations based on the position of the carbon atoms in the octahedral sites. The theoretical lattice parameters were obtained by averaging the corresponding supercell sizes after full lattice relaxation. In Fig. 4 we compare calculated lattice parameters *a* and *c*, as well as the tetragonal distortion *c/a* with experimental data. We see that the calculated lattice parameter *a* of two configurations, the cubic and partially tetragonal, increase with C content, although the experiment shows the opposite trend. In contrast, the fully tetragonal configuration exhibits a decrease of the lattice parameter along the *a*-axis, which agrees with experiment. The calculated *c*-axis (Fig. 4b) increases with carbon content for all configurations although the experimental values are closer to those for cubic and partially tetragonal lattices. Interestingly, the experimental *c/a* ratio in Fig. 4c shows better agreement for the calculated fully tetragonal configuration where only the *z* positions in Fig. 1 are occupied with carbon. These results suggest that the experimentally observed phase with tetragonal distortion exhibits the fully or close to fully tetragonal configuration.

Fig. 5 shows theoretical mixing energy H_{mix} of W–C solid solutions at T = 0 K. The values of H_{mix} calculated with reference to WC carbide are higher compared to those calculated with reference to graphite: $H_{mix}^{carbide} > H_{mix}^{graphite}$, that is due to the stability of the carbide WC phase with respect to pure W and pure C (graphite). The supercells with tetragonal configuration of C atoms have the lowest mixing energy, while the cubic configuration has the highest energy. The mixing energy of partially tetragonal supercell is in-between. The energy difference between three supercells gradually increases with C concentration. This result indicates that tetragonal distortions in the W–C solid solutions favor dissolution of C atoms in W. We should note that all studied configurations demonstrate positive values of mixing energy, which indicates that W–C solid solutions are thermodynamically metastable at T = 0 K. In fact, the experimental results strongly support that a metastable supersaturated solid solution is formed indeed. The theoretical results confirm that the presence of C interstitials increases the stability of the tetragonal configuration.

Carbon interstitials induce local atomic displacements of W atoms from their ideal bcc positions. In Fig. 6a we plot the average

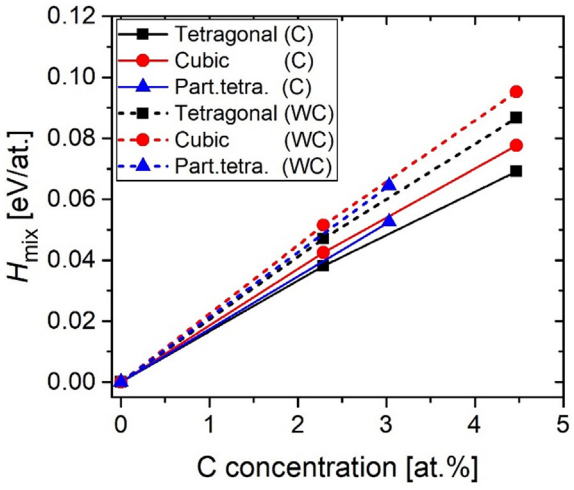

Fig. 5. The mixing energies of W–C solid solutions as functions of C concentration. Solid/dotted lines correspond to the mixing energy calculated with respect to graphite/WC carbide.

displacements of W atoms between ideal and relaxed W–C supercells. The atomic displacements increase with C content. The largest atomic displacement of W occurs in the nearest neighborhood of C atoms. In tetragonal supercells the average displacements are lower compared to cubic supercells, although one would expect the opposite result. We should note that the largest local displacements are observed for tetragonal supercells and occur along the *c*-axis (for lattice parameter *c*). On the other hand, the displacements along the *a*-axis are smaller in tetragonal supercells compared to cubic ones. Cubic solid solutions have overall larger values of average atomic displacements. For the supercell with 4.5 at.% C we plot the critical point of charge density, minimum charge density, between W–W and W–C bonds against the corresponding bond lengths (see Fig. 6b). For the tetragonal solid solutions, the 1st NN W–C bonds are slightly longer and have lower charge density due to the larger lattice parameter *c*. For the 2nd NN W–C bonds we see the opposite result: the bonds in the tetragonal supercell are shorter and have a higher charge density because the lattice parameter *a* is smaller. The W–W bonds in both cubic and tetragonal supercells show very similar trends, although the range of W–W bond lengths in the tetragonal solid solutions is slightly broader.

According to Fig. 6b the bond length between the nearest W–C pairs (in the 1st NN) should increase with tetragonal distortion, creating more room for other C interstitials. Thus, the occupation of certain octahedral positions, along the *c*-axis, becomes energeti-

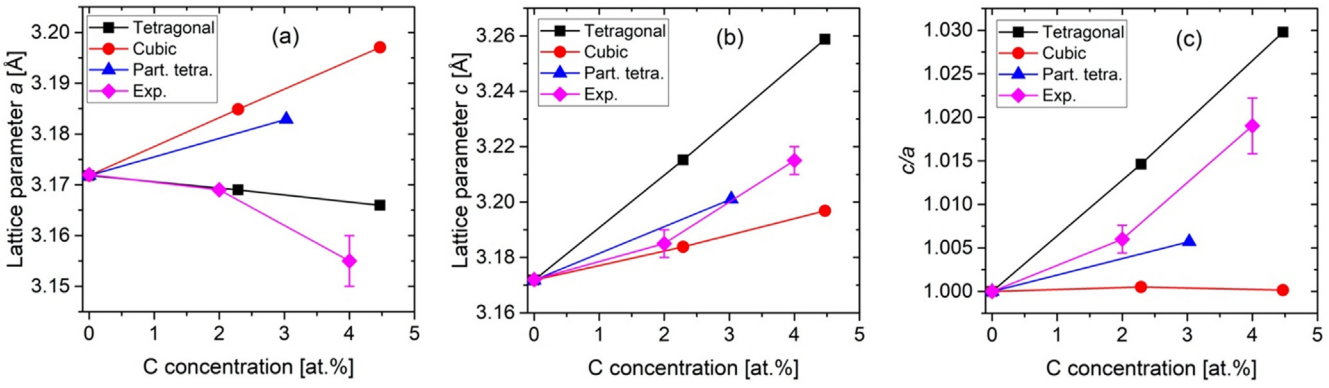

Fig. 4. Theoretical and experimental values of (a,b) lattice parameters *a* and *c*; (c) tetragonal distortion ratio *c/a* of W–C solid solutions as a function of C concentration.

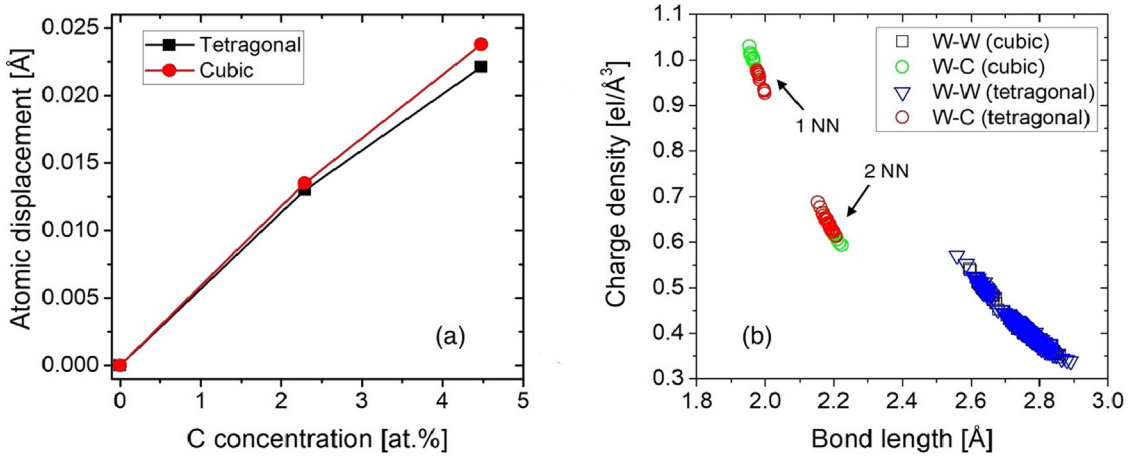

Fig. 6. (a) Average displacement of W atoms between ideal and relaxed W–C supercells. (b) Charge density at critical point between W–W and W–C bonds versus the bond lengths in supercell with 4.5 at.% C.

cally more favorable. This may explain why the H_{mix} difference between tetragonal and cubic configurations becomes larger with increasing C content. Moreover, Fig. 6a shows that average atomic displacements of W atoms off the ideal positions should be smaller in the tetragonal lattice, meaning that less energy is required to introduce C atoms into the tetragonal lattice. As a result, the mixing enthalpy for the tetragonal W–C supercells is lower in comparison to cubic supercells. However, there is the entropy factor, which originates from the configurational disorder of C atoms. For the cubic configuration, C atoms randomly occupy the octahedral positions in all three crystallographic directions, whereas the fully tetragonal configuration demonstrates some sort of "partial order" due to preferential occupation of C atoms in only one direction. Therefore, the entropy of the cubic configuration is higher, and from the thermodynamic point of view one can expect stabilization of the cubic configuration at elevated temperatures due to the entropy factor. Our evaluation shows that entropy driven transition between tetragonal and cubic configurations should occur at ~ 1800 K, which is much higher than the deposition temperature of the studied samples (600 K).

The single-crystal elastic constants C_{ij} of cubic and tetragonal supercells are plotted in Fig. 7. For a cubic crystal, the elastic constant C_{11} is related to the elastic response to the uniaxial strain $(100)\langle 100\rangle$, while C_{12} and C_{44} constants characterize the shear stresses induced by $(110)\langle 100\rangle$ and $(010)\langle 100\rangle$ stains, respectively. The results show that carbon in W decreases the C_{11} and C_{44} constants and increases the C_{12} constant. The differences in elastic constants between three types of C configurations gradually increase with C content. Obviously, this can be explained by the gradual change in the symmetry: the larger tetragonal distortion is, the larger is the difference between cubic and fully tetragonal supercells. Comparison with experimental elastic constants for pure bcc W [37,38] shows that our calculations overestimate the C_{11} constant by ~ 20 GPa and underestimate the C_{12} and C_{44} constants by ~ 10 GPa and ~ 18 GPa, respectively. These differences are 4%, 5%, and 11% respectively, which is well within the typical accuracy margins of the DFT calculations.

Due to the lower symmetry, the tetragonal W–C supercells have three additional elastic constants: C_{13}, C_{33} and C_{66}. However, at the low carbon region where the tetragonal distortion is small one can see that $C_{33} \approx C_{11}$, $C_{13} \approx C_{12}$, and $C_{66} \approx C_{44}$ (see Fig. 5). At higher C concentrations where the tetragonal elastic constants become larger, one can see that $C_{33} > C_{11}$, $C_{13} > C_{12}$ and $C_{66} > C_{44}$.

Fig. 8 shows the bulk modulus B of W–C solid solutions determined by both Birch-Murnaghan EOS and Voight-Reuss-Hill averaging. Both methods give similar trends of bulk modulus as a function of C content, which confirms the reliability of C_{ij} calculations. Bulk modulus determined from the Voight-Reuss-Hill averaging is ~ 1–2 GPa higher (<1%) than the one from the EOS, which is acceptable numerical error. As for the different W–C configurations, the cubic solid solutions demonstrate a slightly lower bulk modulus compared to the fully tetragonal ones. This difference increases with carbon content, although the effect of carbon on B modulus is weak. The bulk modulus of partially tetragonal supercell is in-between the values for cubic and fully tetragonal supercells. In case of pure W there is a good agreement between calculated and experimental B values [39,40]. We should note that in determining the Young's modulus, $E = 9BG/(3B + G)$, we used the bulk modulus obtained from EOS. Calculated shear modulus G of W–C solid solutions is plotted in Fig. 8b. For both tetragonal and cubic configurations, the shear modulus decreases from 158 GPa to ~ 146 GPa when the carbon content increases up to 4.5 at.%. The difference in G modulus between tetragonal and cubic supercells is less than 1 GPa.

The calculated Pugh's ratio B/G of W–C solid solutions is plotted in Fig. 9a. The B/G value is a phenomenological relation, which is often used in the literature to evaluate the tendency to brittleness or ductility in materials [41]. High values of B/G ratio are supposed to indicate the ductility of materials, whereas low values correspond to brittle materials. The B/G value separating ductile and brittle materials is often set to $B/G = 1.75$. For all three supercell configurations the B/G ratio increases with carbon content. This in turn indicates that carbon should improve the ductility of tungsten which in fact is supported by the experimental data from Ref. [18] where no brittle failure was observed in compression tests. The calculations show that cubic supercells have a slightly increased B/G ratio.

In Fig. 9b we compare the experimental and theoretical Young's modulus E of W–C solid solutions. The calculations show that addition of 4.5 at.% carbon decreases the E modulus of tungsten from 405 GPa to ~ 380 GPa. Both G and E moduli show very similar trends as a function of C content; and similar to the G modulus, the E modulus of tetragonal supercell is slightly higher than the one of cubic supercell. For pure bcc W the theoretical calculation of E agrees well with previously reported experimental data [42,43]. The E modulus calculations are in good agreement with our nanoindentation measurements. The experimental values are a bit higher ~ 420 GPa (most likely due to substrate effects [44]) and the decrease is not as pronounced as in the calculations. The experimental data by Fritze et al. [18] and Refs. [45–47] show that

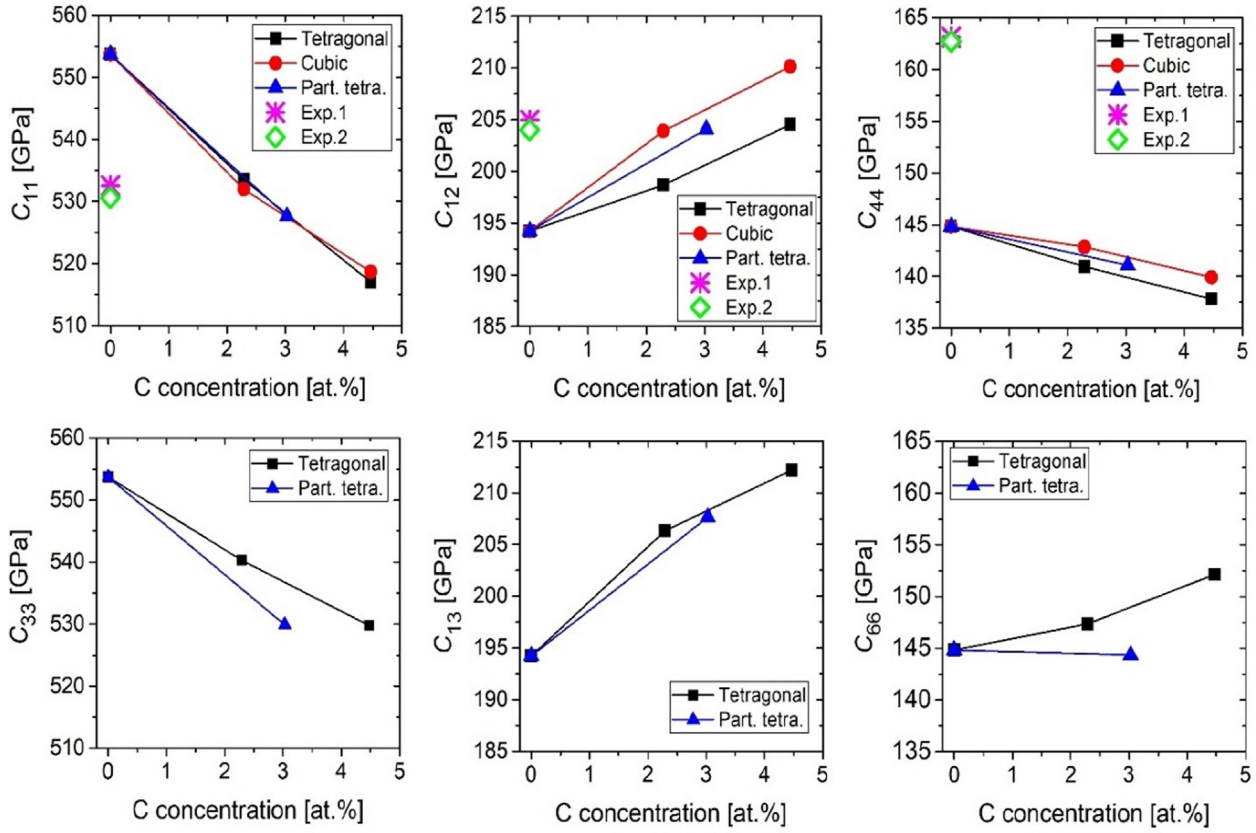

Fig. 7. Elastic constants of W–C solid solutions versus C concertation. Experimental results for pure bcc tungsten are taken from Refs. [39,40] and shown for comparison.

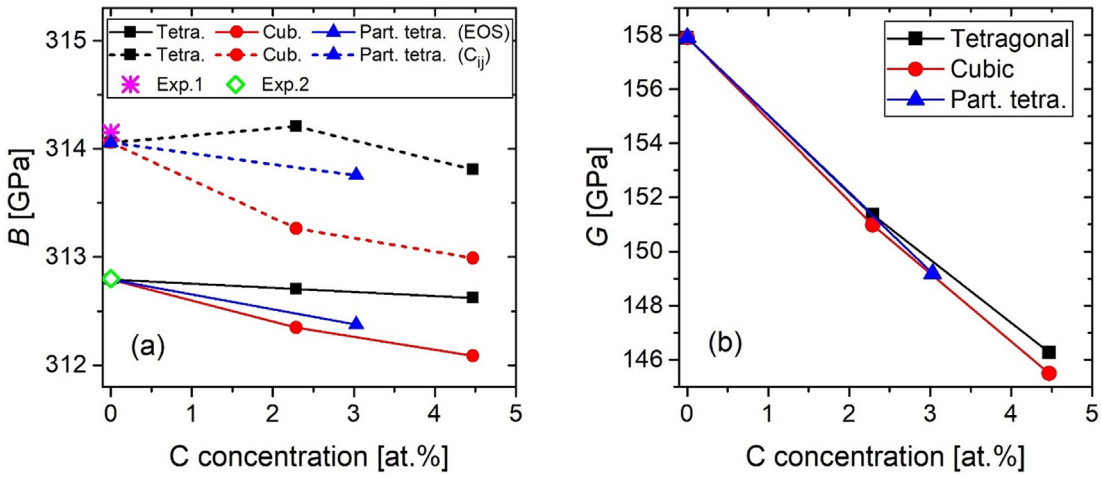

Fig. 8. Concentration dependence of (a) bulk and (b) shear moduli of W–C solid solutions. Bulk modulus was determined using the Voight-Reuss-Hill averaging (dashed lines) and EOS (solid lines). Experimental results for pure tungsten are taken from Refs. [39,40] and shown for comparison.

p-element supersaturated (C, N and B) W films exhibit hardness values between ~ 19 GPa and ~ 28 GPa compared to pure W films which are ~ 13 GPa hard. The high hardness of the pure W films is caused by the nanocrystalline microstructure. The literature overview also shows that p-element supersaturated W films are ~ 10 GPa harder than pure W films with comparable grain size which was explained by a combination of solid solution strengthening and increased dislocation density [18]. The formation of the supersaturated body centered tetragonal (bct) phase can contribute to the increased hardness by a combination of two effects. (i) The bct phase is per-se harder than the bcc phase which can be compared to the Fe-C system where the martensite is harder than the ferrite [16]. (ii) The formation of a dual phase (bcc + bct) microstructure. The increase of hardness due to the formation of the bct phase cannot be estimated by Chen's model ($H_V = 2\left(G^3/B^2\right)^{0.585} - 3$) [48] since it only gives a negligibly small difference in hardness between tetragonal and cubic configurations. This indicates that one cannot only use the difference in the polycrystalline elastic moduli at a fixed C concentration to analyze the effect of lattice distortion on the mechanical properties of W–C solid solutions. An estimation of hardness using theoretical

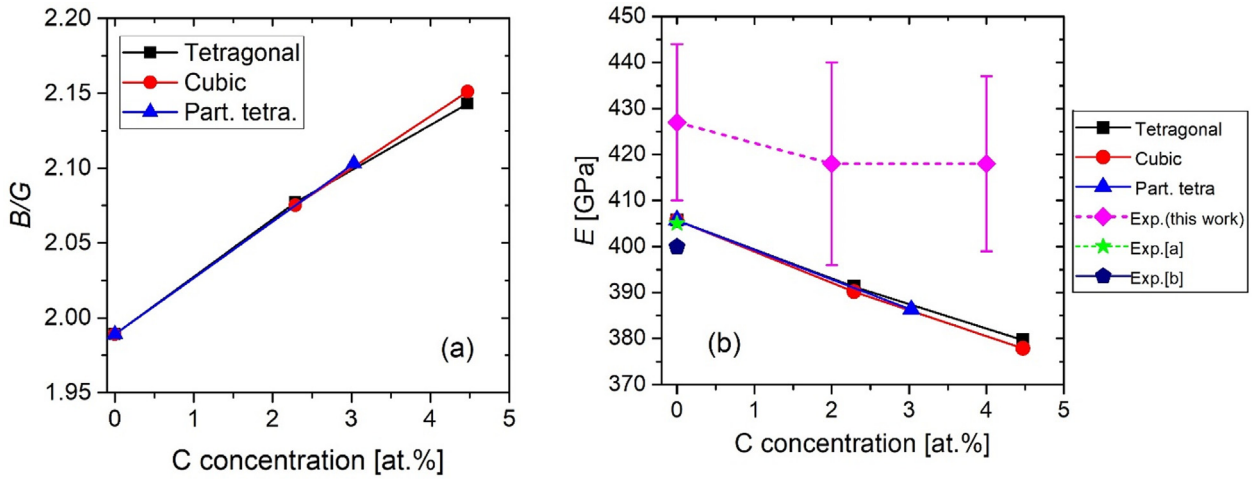

Fig. 9. Pough's ratio (a) and *E* modulus (b) of W–C solid solution as a functions of C concentration. The dashed line denotes our experimental data on *E* modulus. The additional experimental results for pure W are taken from Refs. [40,41] and shown for comparison.

polycrystalline moduli and Chen's empirical model, $H_V = 2\left(G^3/B^2\right)^{0.585} - 3$, shows that addition of 4.48 at.% C reduces the hardness of tungsten from 13.8 GPa to 11.9 GPa, i.e., carbon softens the W–C solid solutions which also can be seen in *E*-modulus calculations. Experimental data on hardness reported earlier in Ref.[18] demonstrate an opposite trend: the hardness of tungsten films increases from 13 GPa to 24 GPa with addition of 4 at.% C. Obviously, our theoretical estimation of hardness does not account for effects such as grain refinement and an increased dislocation density which are present in experimental W–C films. It is well known that grain boundaries act as obstacles to dislocation motion because they separate regions with different crystallographic orientations; and the dislocations tend to pile-up at grain boundaries. Therefore, with a grain refinement one should expect an increased hardness for W–C solid solutions. In addition, one should consider the increase of the C concentration favoring solid solution hardening and how the local atomic displacements and symmetry change affect the dislocation split system, which defines one of the hardening mechanisms in the solid solutions. Thus, this work demonstrates that the Chen's model of hardness is limited and does not account for the microstructure and solution hardening effects listed above, thus it is not supposed to reproduce the hardening of W–C films observed experimentally.

4. Conclusions

We have investigated if a tetragonal distortion of the bcc lattice is possible in W films with a supersaturated carbon content. W–C films with 0 at.%, ~2 at.% and ~ 4 at.% C were synthesized with magnetron sputtering. The ψ–2θ diffraction experiments on the films confirm that a tetragonal distortion is indeed present for the C containing films. The distortion of the lattice was seen as a split between the 200/020 and 002 peaks in the ψ–2θ maps; the distortion increased with higher carbon contents. DFT calculations of the mixing enthalpy suggest that the solid solutions are metastable and that a fully tetragonal configuration is the most stable configuration for the W–C solid solutions. The energy difference between tetragonal and cubic configuration increases with increased C content. Even though H_{mix} is positive, the tetragonal distortions decrease the energy costs for a formation of metastable supersaturated solid solution as compared to the cubic configuration. As the solubility depends exponentially on the energy cost, the observed distortions have a significant influence on the possibility to grow supersaturated W films and in this way to affect their properties.

The calculations show that addition of 4.5 at.% C decreases the *E*-modulus of W from 405 GPa to 385 GPa, which is in good agreement with the nanoindentation measurements, where the addition of 4 at.% C decreases *E*-modulus from 427 GPa to 420 GPa. Our previous study has shown that the pure W film is ~ 13 GPa hard, while the film containing ~ 4 at.% is around ~ 24 GPa hard. The increase of hardness was explained by a combination of grain refinement strengthening, solid solution strengthening and increased dislocation density. The formation of the body centered tetragonal phase can, next to the three above mention mechanisms, also contributes to the very high hardness (~24 GPa) of the W–C films. We propose that the formation of films with such distorted lattices can be an effective way to design properties of not only W films but also other metals with a bcc lattice.

Declaration of Competing Interest

The authors declare that they have no known competing financial interests or personal relationships that could have appeared to influence the work reported in this paper.

Acknowledgements

This work was supported by the Knut and Alice Wallenberg Foundation (Wallenberg Scholar Grant No. KAW-2018.0194) and the Swedish Research Council (VR) Project No. 2018-04834. Support from the Swedish Government Strategic Research Area in Materials Science on Functional Materials at Linköping University, Faculty Grant SFOMatLiU No. 2009 00971 is acknowledged. B.A. acknowledges financial support from the Swedish Foundation for Strategic Research through the Future Research Leaders 6 program, FFL 15-0290 and from the Swedish Research Council (VR) through Grant No. 2019-05403. Theoretical analysis of the results of electronic structure calculations was funded by RFBR, Project No. 20-02-00178. Calculations were performed using supercomputer resources provided by the Swedish National Infrastructure for Computing (SNIC), partially funded by the Swedish Research Council through grant agreement No. 2018-05973, at the National Supercomputer Center (NSC).

Data availability

The data supporting the finding of this study is available at: https://data.openmaterialsdb.se/wctmd/

References

[1] G.H. Aylward, T.J.V. Findlay, SI Chemical Data, sixth ed., John Wiley & Sons, 2013.
[2] O. Torrents Abad, J.M. Wheeler, J. Michler, A.S. Schneider, E. Arzt, Temperature-dependent size effects on the strength of Ta and W micropillars, Acta Mater. 103 (2016) 483–494, https://doi.org/10.1016/j.actamat.2015.10.016.
[3] O. El-Atwani, E. Esquivel, E. Aydogan, E. Martinez, J.K. Baldwin, M. Li, B.P. Uberuaga, S.A. Maloy, Unprecedented irradiation resistance of nanocrystalline tungsten with equiaxed nanocrystalline grains to dislocation loop accumulation, Acta Mater. 165 (2019) 118–128, https://doi.org/10.1016/j.actamat.2018.11.024.
[4] O. El-Atwani, J.A. Hinks, G. Greaves, J.P. Allain, S.A. Maloy, Grain size threshold for enhanced irradiation resistance in nanocrystalline and ultrafine tungsten, Mater. Res. Lett. 5 (5) (2017) 343–349, https://doi.org/10.1080/21663831.2017.1292326.
[5] R.W. Harrison, On the use of ion beams to emulate the neutron irradiation behaviour of tungsten, Vacuum. 160 (2019) 355–370, https://doi.org/10.1016/j.vacuum.2018.11.050.
[6] J. Knaster, A. Moeslang, T. Muroga, Materials research for fusion, Nat. Phys. 12 (5) (2016) 424–434.
[7] L. Romaner, C. Ambrosch-Draxl, R. Pippan, Effect of rhenium on the dislocation core structure in tungsten, Phys. Rev. Lett. 104 (2010) 1–4, https://doi.org/10.1103/PhysRevLett.104.195503.
[8] J. Kappacher, A. Leitner, D. Kiener, H. Clemens, V. Maier-Kiener, Thermally activated deformation mechanisms and solid solution softening in W-Re alloys investigated via high temperature nanoindentation, Mater. Des. 189 (2020) 108499, https://doi.org/10.1016/j.matdes.2020.108499.
[9] D. Scheiber, R. Pippan, P. Puschnig, L. Romaner, Ab initio search for cohesion-enhancing impurity elements at grain boundaries in molybdenum and tungsten, Model. Simul. Mater. Sci. Eng. 24 (8) (2016) 085009, https://doi.org/10.1088/0965-0393/24/8/085009.
[10] P. Gustafson, A Thermodynamic Evaluation of the C-Fe-W System, Metall. Mater. Trans. A. 18 (2) (1987) 175–188, https://doi.org/10.1007/BF02825699.
[11] B. Gludovatz, S. Wurster, T. Weingärtner, A. Hoffmann, R. Pippan, Influence of impurities on the fracture behaviour of tungsten, Philos. Mag. 91 (22) (2011) 3006–3020, https://doi.org/10.1080/14786435.2011.558861.
[12] J. Veverka, M. Vilémová, Z. Chlup, H. Hadraba, F. Lukáč, Š. Csáki, J. Matějíček, J. Vontorová, T. Chráska, Evolution of carbon and oxygen concentration in tungsten prepared by field assisted sintering and its effect on ductility, Int. J. Refract. Met. Hard Mater. 97 (2021) 105499, https://doi.org/10.1016/j.ijrmhm.2021.105499.
[13] N. Castin, A. Dubinko, G. Bonny, A. Bakaev, J. Likonen, A. De Backer, A.E. Sand, K. Heinola, D. Terentyev, The influence of carbon impurities on the formation of loops in tungsten irradiated with self-ions, J. Nucl. Mater. 527 (2019) 151808, https://doi.org/10.1016/j.jnucmat.2019.151808.
[14] Y. Pauleau, P.h. Gouy-Pailler, Very hard solid-solution-type tungsten-carbon coatings deposited by reactive magnetron sputtering, Mater. Lett. 13 (2-3) (1992) 157–160, https://doi.org/10.1016/0167-577X(92)90129-8.
[15] P.h. Gouy-Pailler, Y. Pauleau, Tungsten and tungsten–carbon thin films deposited by magnetron sputtering, J. Vac. Sci. Technol. A Vacuum, Surfaces, Film. 11 (1) (1993) 96–102, https://doi.org/10.1116/1.578725.
[16] J.-P. Palmquist, Z.s. Czigany, M. Odén, J. Neidhart, L. Hultman, U. Jansson, Magnetron sputtered W-C films with C60 as carbon source, Thin Solid Films. 444 (1-2) (2003) 29–37, https://doi.org/10.1016/S0040-6090(03)00937-4.
[17] M. Ohring, Material Science of Thin Films, second ed., 2002. 10.1016/B978-012524975-1/50000-8.
[18] S. Fritze, M. Chen, L. Riekehr, B. Osinger, M.A. Sortica, A. Srinath, A.S. Menon, E. Lewin, D. Primetzhofer, J.M. Wheeler, U. Jansson, Magnetron sputtering of carbon supersaturated tungsten films – A chemical approach to increase strength, Mater. Des. 208 (2021) 109874, https://doi.org/10.1016/j.matdes.2021.109874.
[19] S. Fritze, H. Aboulfadl, R. Hahn, P.H. Mayrhofer, U. Jansson, M. Thuvander, Elemental Distribution and Fracture Toughness of W-C thin films, n.d.
[20] C. Hammond, The Basics of Crystallography and Diffraction, fourth ed., Oxford University Press, 2015. 9780198738688.
[21] Y. Wang, S. Curtarolo, C. Jiang, R. Arroyave, T. Wang, G. Ceder, L.-Q. Chen, Z.-K. Liu, Ab initio lattice stability in comparison with CALPHAD lattice stability, Calphad Comput. Coupling Phase Diagrams Thermochem. 28 (1) (2004) 79–90, https://doi.org/10.1016/j.calphad.2004.05.002.
[22] P.E. Blöchl, Projector augmented-wave method, Phys. Rev. B 50 (24) (1994) 17953–17979, https://doi.org/10.1103/PhysRevB.50.17953.
[23] G. Kresse, J. Furthmüller, Efficiency of ab-initio total energy calculations for metals and semiconductors using a plane-wave basis set, Comput. Mater. Sci. 6 (15) (1996) 15–50, https://doi.org/10.1016/0927-0256(96)00008-0.
[24] G. Kresse, J. Furthmüller, Efficient iterative schemes for ab initio total-energy calculations using a plane-wave basis set, Phys. Rev. B 54 (16) (1996) 11169–11186, https://doi.org/10.1103/PhysRevB.54.11169.
[25] G. Kresse, D. Joubert, From ultrasoft pseudopotentials to the projector augmented-wave method, Phys. Rev. B 59 (3) (1999) 1758–1775, https://doi.org/10.1103/PhysRevB.59.1758.
[26] J.P. Perdew, K. Burke, M. Ernzerhof, Generalized Gradient Approximation Made Simple, Phys. Rev. Lett. 77 (18) (1996) 3865–3868, https://doi.org/10.1103/PhysRevLett.77.3865.
[27] H. Hellmann, Einführung in die Quantumchemie, Deuticke, Leipzig (1937), https://doi.org/10.1002/ange.19410541109.
[28] H.J. Monkhorst, J.D. Pack, Special points for Brillouin-zone integrations, Phys. Rev. B 13 (12) (1976) 5188–5192, https://doi.org/10.1103/PhysRevB.13.5188.
[29] A. Zunger, S.-H. Wei, L.G. Ferreira, J.E. Bernard, Special Quasirandom Structures, Phys. Rev. Lett. 65 (3) (1990) 353–356, https://doi.org/10.1103/PhysRevLett.65.353.
[30] A. Ludsteck, Bestimmung der Änderung der Gitterkonstanten und des anisotropen Debye-Waller-Faktors von Graphit mittels Neutronenbeugung im Temperaturbereich von 25 bis 1850°C, Acta Cryst. A 28 (1) (1972) 59–65, https://doi.org/10.1107/S0567739472000130.
[31] F. Birch, Finite elastic strain of cubic crystals, Phys. Rev. 71 (11) (1947) 809–824, https://doi.org/10.1103/PhysRev.71.809.
[32] M.J. Mehl, B.M. Klein, D.A. Papaconstantopoulos, First principles calculations of elastic properties of metals, in: J.H. Westbrook, R.L. Fleischer (Eds.), Intermetallic Compounds: Principles and Practice, vol. 1, John Wiley & Sons (London, 1994, pp. 195–210.
[33] V.I. Razumovskiy, H.K. Yeddu, J. Spitaler, Effect of carbon on elastic properties and microstructure of maraging steel: First-principles and phase-field study, Computational Materials Science 162 (2019) 1–11, https://doi.org/10.1016/j.commatsci.2019.02.023.
[34] W. Voigt, Ueber die Beziehung zwischen den beiden Elasticitätsconstanten isotroper Körper, Annalen der Physik 274 (1889) 573–587. https://onlinelibrary.wiley.com/doi/abs/10.1002/andp.18892741206.
[35] A. Reuss, Berechnung der Fließgrenze von Mischkristallen auf Grund der Plastizitätsbedingung für Einkristalle, ZAMM – J. Appl, Z. angew. Math. Mech. 9 (1) (1929) 49–58, https://doi.org/10.1002/zamm.19290090104.
[36] R. Hill, The elastic behaviour of a crystalline aggregate, Proc. Phys. Soc. Section A 65 (5) (1952) 349–354, https://doi.org/10.1088/0370-1298/65/5/307.
[37] P.H. Mayrhofer, C. Mitterer, L. Hultman, H. Clemens, Microstructural design of hard coatings, Prog. Mater. Sci. 51 (8) (2006) 1032–1114, https://doi.org/10.1016/j.pmatsci.2006.02.002.
[38] D.H. Trinh, T. Kubart, T. Nyberg, M. Ottosson, L. Hultman, H. Högberg, Direct current magnetron sputtering deposition of nanocomposite alumina - zirconia thin films, Thin Solid Films. 516 (23) (2008) 8352–8358, https://doi.org/10.1016/j.tsf.2008.04.040.
[39] F.H. Featherston, J.R. Neighbours, Elastic Constants of Tantalum, Tungsten, and Molybdenum, Phys. Rev. 130 (4) (1963) 1324–1333, https://doi.org/10.1103/PhysRev.130.1324.
[40] D.I. Bolef, J. De Klerk, Elastic Constants of Single-Crystal Mo and W between 77° and 500° K, J. Appl. Phys. 33 (7) (1962) 2311–2314, https://doi.org/10.1063/1.1728952.
[41] S.F. Pugh, Relations between the elastic moduli and the plastic properties of polycrystalline pure metals, Philos. Mag. Ser. 745 (1954) 823, https://doi.org/10.1080/14786440808520496.
[42] G. Simmons, H. Wang, Single Crystal Elastic Constants and Calculated Aggregate Properties: A Handbook, M.I.T. Press, Cambridge, MA, 1971.
[43] E. Grünwald, R. Nuster, R. Treml, D. Kiener, G. Paltauf, R. Brunner, Young's Modulus and Poisson's Ratio Characterization of Tungsten Thin Films via Laser Ultrasound, Materials Today: Proceedings 2 2 (8) (2015) 4289–4294, https://doi.org/10.1016/j.matpr.2015.09.015.
[44] R. Saha, W.D. Nix, Effects of the substrate on the determination of thin film mechanical properties by nanoindentation, Acta Mater. 50 (1) (2002) 23–38, https://doi.org/10.1016/S1359-6454(01)00328-7.
[45] L. Yang, K. Zhang, M. Wen, Z. Hou, C. Gong, X. Liu, C. Hu, X. Cui, W. Zheng, Highly hard yet toughened bcc-W coating by doping unexpectedly low B content, Sci. Rep. 7 (2017) 1–8, https://doi.org/10.1038/s41598-017-09807-9.
[46] L. Yang, C. Liu, M. Wen, X. Dai, Y. Zhang, X. Chen, K. Zhang, Small atoms as reinforced agent for both hardness and toughness of Group-VIB transition metal films, J. Alloys Compd. 735 (2018) 1105–1110, https://doi.org/10.1016/j.jallcom.2017.11.208.
[47] D. Javdošňák, J. Musil, Z. Soukup, S. Haviar, R. Čerstvý, J. Houska, Tribological properties and oxidation resistance of tungsten and tungsten nitride films at temperatures up to 500 °C, Tribol. Int. 132 (2019) 211–220, https://doi.org/10.1016/j.triboint.2018.12.019.
[48] X.-Q. Chen, H. Niu, D. Li, Y. Li, Modeling hardness of polycrystalline materials and bulk metallic glasses, Intermetallics 19 (9) (2011) 1275–1281, https://doi.org/10.1016/j.intermet.2011.03.026.